J. Fluid Mech. (1987), *vol.* 182, *pp.* 235–254
Printed in Great Britain

Speckle measurements of convection in a liquid cooled from above

By R. MEYNART†
Service des Milieux Continus, Université Libre de Bruxelles, Belgium

P. G. SIMPKINS AND T. D. DUDDERAR
AT&T Bell Laboratories, Murray Hill, NJ 07974, USA

(Received 2 July 1986)

Buoyancy-driven recirculation in a liquid-filled rectangular cavity cooled from above is shown to be locally modulated by an unstable thermal layer at the surface. Interferometric observations suggest that fluctuations that occur in a plume descending through the upper liquid layers are of the type described by Howard (1964) and by Krishnamurti & Howard (1981). Temperature measurements across the surface layer are in reasonable agreement with the diffusive heat-conduction model, but indicate that near the plume the fluid is cooler than elsewhere. Quasi-steady measurements of the velocity distribution in the upper regions of the cavity were made using multiple-exposure laser speckle velocimetry. Interrogation of the specklegrams with a Young's fringe technique yields a velocity-vector field of about two thousand elements. These data are used to calculate the corresponding velocity components and estimates of the vorticity distribution. The results compare favourably with measurements recorded directly from Fourier filtering methods.

1. Introduction

This paper is concerned with the convective motion that develops in a deep liquid layer when it is heated by isothermal vertical walls and it is cooled from either the upper, or both horizontal surfaces. When thermal equilibrium is achieved, the motion in a two-dimensional cavity consists of two recirculation cells separated by a descending plume that may or may not penetrate to the bottom. The types of flow that occur are dependent on the Rayleigh number R and the aspect ratio L (length/depth) of the enclosure. Here R is defined in terms of the cavity height and the temperature difference between the sidewalls and the upper surface. If the temperature of the lower surface is different from that of the sidewalls another parameter, the dimensionless temperature Θ, also influences the flow field. By definition $\Theta = (T-T_t)/(T_w-T_t)$, where T is the temperature and the subscripts t and w refer to the upper surface and sidewall conditions, respectively. In general, changes in the Prandtl number may also have an effect, but here that parameter is taken to be fixed.

When $R \gg 1$ and $L \gg 1$ the flow field corresponds to the situation studied by meteorologists and oceanographers, see e.g. Willis & Deardorff (1979). The case $R \gg 1$, $L \ll 1$ has been examined by Lighthill (1953) and others with regard to thermosyphon effects, and it was noted that, in some circumstances, a stagnant zone can exist at

---

† Present address: ACEC, 6000 Charleroi, Belgium.

the bottom of the cavity. Similar features have been observed in crystal-growth simulations by Miller & Pernell (1981) and by geophysicists interested in magma convection (Jaupart, Brandeis & Allègre 1984). Since those studies dealt with liquid layers, they differed from the model considered by Lighthill because the top of the layer can be a stress-free surface. Observations of natural convection in an unbounded liquid layer cooled from above suggest that motion occurs in the form of plunging sheets or columns of negatively buoyant material, see e.g. Spangenberg & Rowland (1961), Katsaros *et al.* (1977) and Foster & Waller (1985). These characteristics are complementary to those described by Elder (1968) for an unstable thermal interface heated from below. In both situations the motion is a consequence of an adverse temperature gradient that develops from the interface by molecular diffusion. As the thickness of this diffusive layer grows, it eventually attains a critical value, after which disruptive instabilities occur. Howard (1964) originally proposed a model of this type based on the well-known solution of the one-dimensional heat-conduction equation. A time-dependent stability analysis of the problem has been reported by Foster (1965).

The experiments to be described are two-dimensional simulations of the Czochralski method for growing monolithic single crystals of the type used in the semi-conductor industry. Flow-field variations due to the crystal rotation used in the manufacturing process are ignored in the present experiments, which deal exclusively with an unobstructed free surface. All the results described here are for conditions in which the recirculation zones did not fill the cavity and thus an almost stagnant layer existed near the bottom. Disruptive instabilities, associated with the unstable thermal layer near the surface, superimpose an intermittency on to the steady recirculation in the enclosure. This unsteadiness causes the negatively buoyant plume to weave back and forth, and periodically to plunge deeper into the fluid. Quantitative measurements of the intermittency in the plume are obtained from a wavefront-shearing interferometer. Because the timescale of the periodicity is relatively large, it is possible to obtain quasi-steady flow-field information in the upper region of the enclosure.

The terminology 'laser speckle velocimetry' to describe the experimental procedure is generic, in the same sense that LDV is used to cover a broad range of operational modes. In the current work the speckles do not arise from the coherent properties of the illumination, but rather they are discrete images of the seeding. However, the multiplicity of exposures used in the present procedure increases the image density, which leads to an enhancement of the signal-to-noise ratio beyond that found with double-exposure techniques. Two methods for determining the velocity distribution from multiply exposed speckle photographs are described in the following sections. The first of these, which yields the magnitude and the orientation of the local velocity vector, is a point-wise optical scanning procedure which utilizes the Young's fringe method of analysing the speckle photograph. An automated version of this approach yields an array of vector information from which other details of the flow may be found. A second technique provides full-field distributions of the velocity components by optically (Fourier) filtering the speckle photographs. The fringe patterns may be recorded either photographically or on videotape for later analysis.

2. Thermal-interface analyses

An idealized model for the development of an unstable thermal sublayer was proposed by Howard (1964). The model is based on the assertion that an atmospheric thermal can be characterized by a bimodal behaviour in which the eruptive phase is much shorter than the gestation period (Townsend 1959). Howard argued, therefore, that in the initial stages of development the sub-layer is dominated by thermal conduction, and that the short-lived buoyant eruption depletes the layer of warm fluid so that the process can be repeated.

Consider a motionless fluid layer of thickness h, subjected to a sudden temperature defect ΔT at the upper surface $z = 0$ at time $t = 0$, where ΔT is defined as $(T - T_\infty)/(T_t - T_\infty)$. T_∞ refers to the undisturbed fluid temperature far from the surface. In this case the governing equations reduce to the one-dimensional heat-conduction equation, which has a similarity solution

$$f(\eta) = \operatorname{erfc} \eta, \tag{2.1}$$

where $\eta = z(4\kappa t)^{-\frac{1}{2}}$ is the similarity variable and κ is the thermal diffusivity; see Carslaw & Jaeger (1959). If a thermal is formed in a time $t^* \ll h^2/\kappa$, the diffusion time, the temperature can be averaged over t^* to yield the mean temperature profile and the mean heat flux. The mean temperature is given by

$$\bar{T} = \Delta T\{\operatorname{erfc} \xi(1+2\xi^2) - 2\pi^{-\frac{1}{2}}\xi \exp(-\xi^2)\}, \tag{2.2}$$

where $\xi = z(4\kappa t^*)^{-\frac{1}{2}}$.

When the upper-surface boundary condition is one of constant flux Q, the transformation

$$T = Q(\kappa t)^{\frac{1}{2}} K^{-1} \theta(\eta), \tag{2.3}$$

where K is the thermal conductivity, can be used to give a corresponding solution

$$\theta(\eta) = 2\{\pi^{-\frac{1}{2}} \exp(-\eta^2) - \eta \operatorname{erfc} \eta\} \tag{2.4}$$

(Carslaw & Jaeger 1959, p. 75). In this case the mean temperature profile over the period t^* becomes

$$\bar{T} = \tfrac{2}{3} Q z K^{-1}\{\pi^{-\frac{1}{2}}(\xi + \xi^{-1}) \exp(-\xi^2) - (\xi^2 + \tfrac{3}{2}) \operatorname{erfc} \xi\}, \tag{2.5}$$

and, on the upper surface,

$$\bar{T}_t = \tfrac{4}{3} Q K^{-1} \left(\frac{\kappa t^*}{\pi}\right)^{\frac{1}{2}}. \tag{2.6}$$

These results are strictly for a deep, motionless liquid layer and suggest a scale thickness for the thermal layer of $\delta = (4\kappa t^*)^{\frac{1}{2}}$. When the value of δ is such that the Rayleigh number R, based on δ, reaches a critical value the adverse temperature gradient causes an instability to develop. Howard noted that the determination of t^* is not easy because the precise value of R_{crit} is unknown for deep layers. However, if R_{crit} is taken to be 10^3, typical of the case of the fixed-free-boundary condition for the Rayleigh–Bénard experiment, the estimated value for t^* is about 30 s. This result is, of course, only an estimate of the gestation period needed for a thermal layer to grow and, as Howard and others have noted, is strictly not correct. Data from the experiments to be presented do show good agreement with the estimated value of t^* (Simpkins 1985), but it must be remembered that the present situation is not one of a motionless layer. Currently there do not appear to be any analytical models of the onset of such an instability when convective effects are also present. Most analyses do not account for constraints imposed by vertical walls, and hence the recirculation is not considered.

Recently, Howard & Krishnamurti (1986) have described a model, based on truncation of the two-dimensional Boussinesq equations, that exhibits some of the characteristics observed in turbulent convection. In particular, bifurcations that arise in the model equations ultimately lead to a time-dependent motion in which tilted transient plumes and a large-scale Lagrangian mean flow occur. Behaviour of this type has been observed experimentally (Krishnamurti & Howard 1981) in shallow water layers, i.e. $L = (l/h) \gg 1$; where l is the layer length and h is the height. The motion associated with the plumes occurs on a lengthscale $O(h)$. Beyond a bifurcation at a Rayleigh number $R^* \approx 2 \times 10^6$, where $R^* = R\Theta$, the motion evolves into one that has drifting tilted plumes and a lengthscale of $O(l)$. Development of the large-scale Lagrangian motion is not relevant to the current work, but the onset of a non-symmetrical tilted state will be discussed further in §6.3.

3. Experimental methods

The experiments were carried out in a modified version of the apparatus described by Simpkins & Dudderar (1981). Figure 1 shows a schematic of the apparatus which consists of a rectangular cavity, with endwalls that can be maintained at a constant, uniform temperature. Identical endwall 'thermodes' were supplied with constant-temperature coolant by a common, thermostatically controlled circulator. Each thermode incorporates an enclosed copper circulation chamber with internal extended surfaces attached at the endwall interior to enhance the thermal coupling and the heat distribution. Copper–constantan thermocouples were used to monitor the inlet and outlet coolant temperatures and the centreline temperature of each endwall about 5 mm above the bottom. A horizontal copper thermode, similarly instrumented and supplied by a separate circulator, provided a uniform, constant-temperature bottom.

Water was used as the test medium in the cavity because its physical properties are similar to those of molten garnet (Miller & Pernell 1981), and because it is suitable for flow-visualization studies. Illumination of a thin vertical plane in the cavity was provided by a 3 W argon-ion laser, the output of which was shaped with a suitable optical system. Light scattered by neutrally buoyant 5 μm polystyrene spheres in the illuminated plane can be recorded as streak images of the flow. These records yield a convenient flow-field visualization, but in general the quantitative information derived from them is limited. Alternatively, if the illumination is periodically interrupted, the velocity distribution throughout the flow can be determined.

Variations in the thermal gradient throughout the cavity were monitored with a wavefront-shearing interferometer. The light source was a 35 mW He–Ne laser, the beam of which was expanded via a spatial filter and collimated with a high-quality doublet lens (accurate to 2λ at 632.8 mm). After passing through the test section the beam was sheared horizontally with a parallel-sided glass plate (10 mm thick, optically flat to $\lambda/10$) oriented at 45° to the vertical plane. In this arrangement the sensitivity of the instrument to changes in the horizontal temperature gradient was 0.03 °C/mm-fringe, but details of the thermal distribution near the vertical walls cannot be measured because of the shearing process. Any flow unsteadiness near the centre of the cell, however, could be observed by localizing the interferometer image on to a small photodiode. Details of the technique have been given by Bryngdahl (1965) and by Oertel & Bühler (1978).

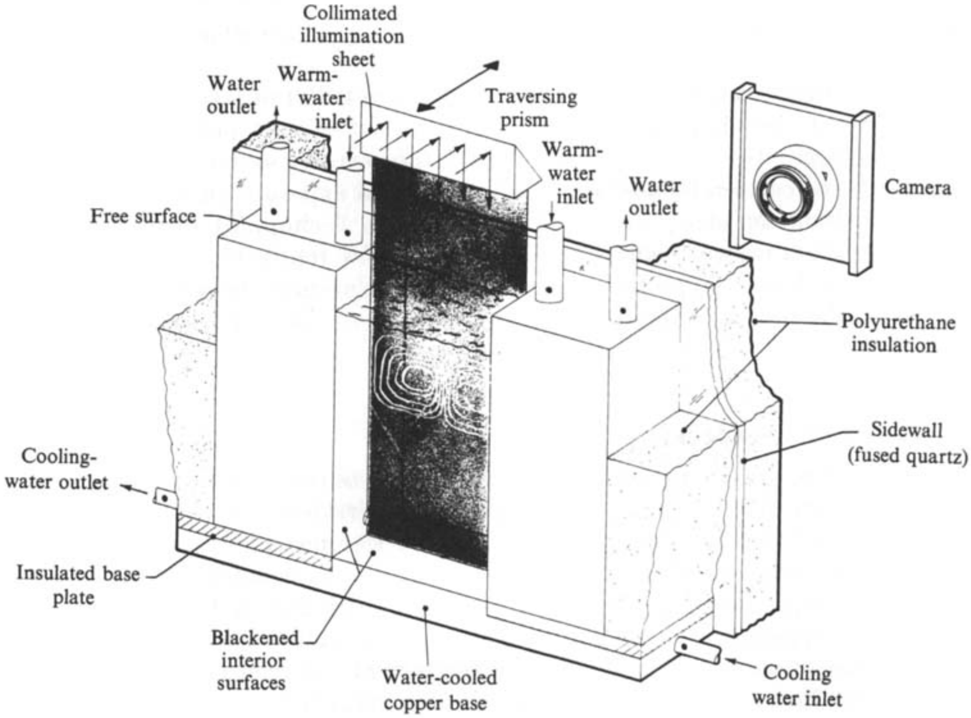

FIGURE 1. Experimental arrangement of the test cell with the near-side insulation omitted for clarity.

4. Acquisition techniques for the velocity field

To ensure that the light intensity scattered by the seeding particles in the flow was optimized, the laser beam was polarized in the plane parallel to the light sheet as it traversed the cavity. It is estimated that the usable length of the shaped beam was 80 mm and that its thickness was 180 ± 60 μm. These estimates assume that the beam intensity distribution is Gaussian and that aberration effects are negligible. Since the water depth is about 50 mm, the power spectral density and the thickness along the optical path in the liquid was therefore reasonably uniform. Control for the multiple-exposure photographs was provided by a mechanical chopper in the form of a rotating slotted wheel.

The photographic equipment consisted of a Nikon F3 camera and a macro 105 mm lens. This particular lens was selected because it is aberration-free for short object–lens distances, and because its long focal length allows pictures of 1/2 magnification to be taken at correspondingly large distances. Relatively large object–lens distances ($3f \approx 300$ mm) help reduce the apparent in-plane displacement of the particles due to the out-of-plane displacement when short-focal-length lenses are used (Asundi & Chiang 1982). Polaroid Polagraph 400 ASA film was used because it has a short processing time, and because the emulsion provides a positive image. The latter is advantageous when the photographs are to be analysed optically, since the signal-to-noise ratio is improved when scattering in the emulsion and its plastic base is suppressed. Comments concerning this effect have been made in Meynart (1983*a*) and by Lourenco & Whiffen (1984) and Pickering & Halliwell (1984). By the same token, the intensity of the central bright spot due to the undiffracted portion of the beam is also reduced considerably. Although the Polaroid film resolution is modest, it is adequate for recording the positions of the 20–30 μm diameter images accurately.

The laser-beam chopper was designed to transmit illumination 5% of the time. Adjustment of the chopping rate and of the laser output power gave pulses of sufficient intensity to ensure discrete images of the particles moving in the illuminated plane. With the camera focused on this plane a total exposure duration was selected to provide about ten sharp images of each particle. A chopping rate was chosen to give a separation between successive images of a few tenths of a mm in the region of maximum velocity. Typically, the maximum displacement between images should be equal to the radius of the interrogation beam used for pointwise data reduction (see §5).

5. Analysis of the speckle photographs

Two optical methods are commonly used to analyse conventional doubly exposed speckle photographs for velocity measurement. The first is a point-by-point procedure which exploits the classical Young's fringe interference phenomenon to provide accurate measurements of the local velocity vector. A second method, the Fourier filtering technique, can be used to obtain the global distribution of the velocity components. Application of both of these methods is described below. Conventional doubly exposed fluid-velocity speckle photographs are inherently difficult to analyse by the optical Fourier filtering technique, and can usually be optically analysed only by the pointwise Young's fringe method; however, it will be demonstrated that the multiple-exposure technique used here has the added advantage of generating speckle photographs of high signal-to-noise ratio which may be analysed by cither method. In addition, the multiple-exposure technique requires much less seeding than that needed for the double-exposure speckle method.

5.1. *Local measurements by the Young's fringe technique*

The speckle photographs were analysed point by point using the optical processor described by Meynart (1983*b*). A low-power He–Ne laser beam was shaped by two plano-convex lenses to produce a beam of diameter $d = 0.35$–0.4 mm in the focal back plane of the second lens, where the photograph is inserted. Light diffracted by the particle images in the photograph is collected by a 150 mm lens, and the squared Fourier transform (the Young's fringes) of the illuminated region is observed in the diffraction halo which forms in the focal back plane. An opaque dot, located on the optical axis in the observation plane, is used to stop the bright undiffracted beam. The fringes were imaged on to a vidicon tube of a TV camera with a 50 mm macro lens. Video images of the fringe field were digitized in 256 × 256 pixels (8 bits per pixel) and transferred to a PDP 11/34 computer for analysis. Translation stages were used to move the speckle photograph for sequential processing of points throughout the entire field.

The principle of generating Young's fringes by the local illumination of a double-exposed photograph of a moving random pattern is well known. In practice, data-reduction methods that use digital techniques are necessary to analyse the many fringe distributions that are generated in any extensive flow-field determination (Meynart 1983*b*). These techniques are outlined briefly below, with a particular emphasis on the specific modifications required to take advantage of the multiple-exposure method.

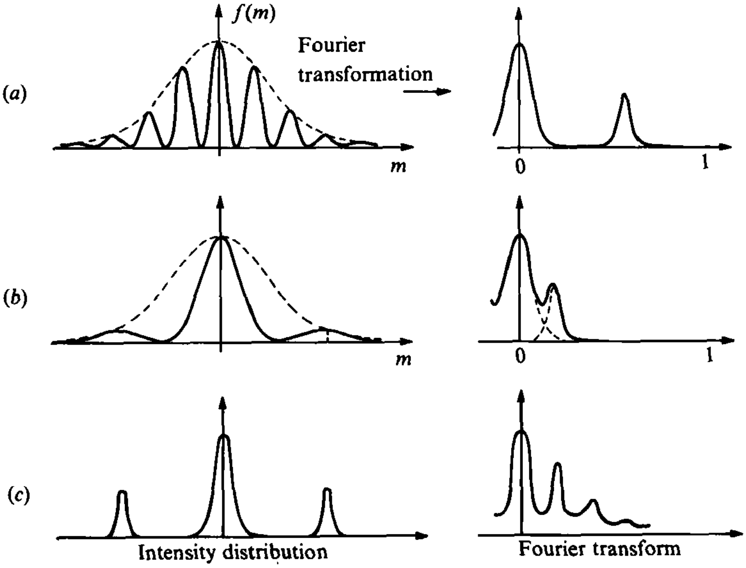

FIGURE 2. Processing of the averaged profile of the fringes. (*a*) Large displacement; (*b*) small displacement (two exposures); (*c*) small displacement (N exposures, $N \gg 2$).

One difficulty in processing noisy fields of straight parallel fringes is to determine their angular orientation α. Normally this procedure would require long computation times, but the measurement can be aided by an operator who adjusts the angular orientation of a cursor that is superimposed on the fringes until the two are parallel. The computer then averages the noisy two-dimensional intensity distribution along the fringe direction to obtain a cleaner one-dimensional signal, $f(m)$, whose period is a measure of one component of the displacement.

Two techniques can be used for measuring the peak frequency of the averaged intensity distribution $f(m)$. If the displacement is large enough to produce five bright fringes (two orders of diffraction) or more, a simple one-dimensional Fourier analysis of $f(m)$ yields a well-defined peak whose location can be accurately measured (figure 2*a*). This approach is unsuitable when the velocity is very low, e.g. if only two faint fringes, in addition to the longest central fringe, can be discerned in the Fourier transform plane. In this case, which is common in double-exposure speckle recordings, the accuracy of the measurement is questionable because of the interaction of the useful peak at the fringe frequency with the low-frequency Gaussian component of the diffraction halo (figure 2*b*). Multiple-exposure recording ensures, however, that the fringes are bright and thin, and that their spacing can be measured directly in $f(m)$; see figure 2(*c*). This phenomenon is, of course, well known and is characterized in numerous texts concerned with the theory of diffraction, e.g. Lipson & Lipson (1969). Examples related specifically to the speckle effect in this regard have been described by Burch & Tokarski (1968), Meynart (1980, 1982) and Lourenco & Whiffen (1984). The present procedure therefore allows very low velocities to be measured accurately, and consequently increases the dynamic range of the measurement. In the present experiments displacements as small as 20 μm (i.e. one particle-image diameter) have been recorded. Thus it is estimated that the dynamic range is about 10:1.

Aberration leads to errors in the measurements by introducing speckle into the fringe fields. For a diffraction-limited point source, the image size $\phi \approx 2.4\lambda(1+m)F$, where λ is the wavelength, m is the magnification and F is the lens f-number. Typically, therefore, with $\lambda \approx 0.5$ µm, $m = 0.5$ and $F = 4$, $\phi \approx 7.2$ µm for an ideal lens. Other aberrations due to scattering between particles, film resolution, transmission through the test cell and overexposure, account for the differences between the above estimate and the observed particle diameters of 20–30 µm. Errors introduced by speckle noise have been discussed by Meynart (1983*b*) with regard to Kodak film. The lower resolution of the Polaroid film used in these experiments is expected to result in displacement errors of about 5 µm and orientation discrepancies perhaps as large as $\pm 2°$. Estimates of the uncertainty in the vertical-displacement component $h_y (= h_x \tan\alpha)$ are given by $\Delta h_y = (h_x^{-1}\Delta h_x + 2\Delta\alpha \operatorname{cosec} 2\alpha)\, h_y$. In a conservative case, $h_x = 100$ µm, $\Delta h_x = 5$ µm, $\alpha = 30°$ and $\Delta\alpha = 2°$, the uncertainty is about 13%. Systematic errors in the computations are expected to add several per cent to this value. Errors introduced by the intensity variation across the diffraction halo are discussed in Appendix A.

5.2. *Global measurement by Fourier filtering*

Use of significantly more than two successive exposures yields bright and thin Young's fringes. The fringe energy density is increased for two reasons: more than two diffracting points contribute to the fringe intensity and this enhanced intensity is concentrated into narrower fringes. Consequently, the signal-to-noise ratio is considerably larger than that of the double-exposure technique. As noted earlier, this improvement is also the key factor in the application of the spatial filtering technique for making global velocity measurements. A useful introduction to spatial filtering and optical-information processing is given by Goodman (1968).

One classical Fourier filtering set-up is shown in figure 3. A lens L_3 of focal length f produces the Fourier transform of the photograph P in the focal back plane where an opaque mask M with a small circular aperture is located. After bandpass filtering by the aperture in M, the lens L_4 performs a second (inverse) Fourier transform and a filtered image of the photograph is reconstructed in its back focal plane I.

The transformation properties of this imaging system can be described by a convolution integral:

$$A(\boldsymbol{r}_\mathrm{i}) = \iint T(\boldsymbol{r}_0)\cdot K(\boldsymbol{r}_\mathrm{i}+\boldsymbol{r}_0)\,\mathrm{d}\boldsymbol{r}_0 = \iint K(\boldsymbol{r}_0)\cdot T(\boldsymbol{r}_0-\boldsymbol{r}_\mathrm{i})\,\mathrm{d}\boldsymbol{r}_0, \tag{5.1}$$

where $\boldsymbol{r}_\mathrm{i}$ and $\boldsymbol{r}_0$ are the coordinates in the image and object planes, $A(\boldsymbol{r}_\mathrm{i})$ is the amplitude of the image, $T(\boldsymbol{r}_0)$ is the object transmittance and $K(\boldsymbol{r}_0)$ is the impulse response of the filter. For a circular aperture of radius a with its centre located in the plane of the mask at $\boldsymbol{r}_\mathrm{i}$ from the optical axis, the impulse response is given by

$$K(\boldsymbol{r}_0) = \exp\left(-2\pi\mathrm{i}\boldsymbol{r}_0\cdot\boldsymbol{f}_0\right)\frac{J_1(2\pi r_0 \Delta f)}{2\pi r_0 \Delta f}, \tag{5.2}$$

where i is the imaginary unit, J_1 is a Bessel function of the first kind, and $\Delta f = a/(\lambda f)$ and $\boldsymbol{f}_0 = \boldsymbol{r}_\mathrm{i}/(\lambda/f)$ are the pass bandwidth and the central spatial frequency of the filter, respectively. Suppose the object is the periodic superposition of N identical patterns, then

$$T(\boldsymbol{r}_0) = \sum_{k=0}^{N-1} C(\boldsymbol{r}_0 - k\boldsymbol{s}), \tag{5.3}$$

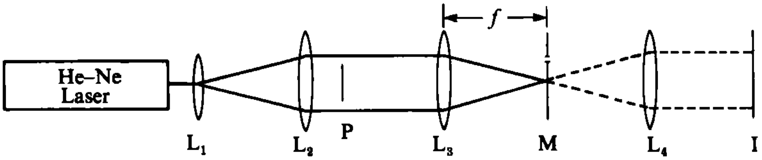

FIGURE 3. Spatial filtering set-up. L$_1$ and L$_2$ are beam expanders; L$_3$, L$_4$, converging lenses; P is the speckle photograph; M an opaque mask with a circular aperture, and I is the image plane.

where $\boldsymbol{s}$ is the displacement between exposures. If the displacement field $\boldsymbol{s}$ is assumed to be continuous, then

$$A(\boldsymbol{r}_\mathrm{i}) = \iint C(\boldsymbol{r}-\boldsymbol{r}_\mathrm{i}) \exp(-2\pi \mathrm{i} k \boldsymbol{f}_0 \boldsymbol{r}) \left[\sum_{k=0}^{N} \exp(-2\pi \mathrm{i} k \boldsymbol{f}_0 \cdot \boldsymbol{s}) \frac{J_1(2\pi \Delta f [\boldsymbol{r}+k\boldsymbol{s}])}{2\pi\Delta f |\boldsymbol{r}+k\boldsymbol{s}|}\right] \mathrm{d}\boldsymbol{r} \quad (5.4)$$

$$= \sum_{k=0}^{N} \exp(-2\pi \mathrm{i} k \boldsymbol{f}_0 \cdot \boldsymbol{s}) \iint C(\boldsymbol{r}-\boldsymbol{r}_\mathrm{i}) \exp(-2\pi \mathrm{i} \boldsymbol{f}_0 \cdot \boldsymbol{r}) \frac{J_1(2\pi\Delta f[\boldsymbol{r}+k\boldsymbol{s}])}{2\pi\Delta f[\boldsymbol{r}+k\boldsymbol{s}]} \mathrm{d}\boldsymbol{r}. \quad (5.5)$$

When the total displacement Nx is smaller than the pass bandwidth of the impulse response ($Nx \leqslant \lambda f/a$), all the integrals contained in (5.5) are identical and

$$A(\boldsymbol{r}_\mathrm{i}) = \left\{\sum_{k=0}^{N-1} -2\pi \mathrm{i} k \boldsymbol{f}_0 \boldsymbol{s}\right\} \left\{\iint C(\boldsymbol{r}-\boldsymbol{r}_\mathrm{i}) \exp(-2\pi \mathrm{i} \boldsymbol{f}_0 \boldsymbol{r}) \frac{J_1(2\pi\Delta f r)}{2\pi\Delta f r} \mathrm{d}\boldsymbol{r}\right\}, \quad (5.6)$$

which is the product of the image of the object $C(\boldsymbol{r}_\mathrm{o})$ and the thin fringes described by the first term. The fringes are bright whenever

$$\boldsymbol{f}_0 \cdot \boldsymbol{s} = \frac{\boldsymbol{r}_\mathrm{f} \cdot \boldsymbol{s}}{\lambda f} = n \quad (n = 0, 1, 2, \ldots).$$

Provided the displacement is not negligible compared to $a/(\lambda f)$, the amplitude, $A(\boldsymbol{r}_\mathrm{i})$, can be described simply by assuming that the image of the object $C(\boldsymbol{r}_\mathrm{o})$ consists of an isolated point. In this case

$$C(\boldsymbol{r}_\mathrm{o}) = \delta(\boldsymbol{r}_\mathrm{o}),$$

and

$$A(\boldsymbol{r}_\mathrm{i}) = \sum_{k=0}^{N} \frac{J_1(2\pi\Delta f[\boldsymbol{r}_\mathrm{i}+k\boldsymbol{s}])}{2\pi\Delta f[\boldsymbol{r}_\mathrm{i}+k\boldsymbol{s}]} \exp(-2\pi \mathrm{i} k \boldsymbol{f}_0 \cdot \boldsymbol{s}). \quad (5.7)$$

Equation (5.7) describes the coherent superposition of N impulse responses of diameter $\approx \lambda f/a$ separated by a constant distance x. Only a limited set of terms contribute appreciably to the total amplitude at any point $\boldsymbol{r}_\mathrm{i} = -b\boldsymbol{s}$. Here b is an integer ($0 \leqslant b \leqslant N-1$) corresponding to the position of a single geometrical image of a particle. These terms are labelled $b-m, \ldots, b+m$ with $(2m+1)x \approx \lambda f/a$. For $\boldsymbol{f}_0 \cdot \boldsymbol{s} = n$, all the terms are of the same sign, while for $\boldsymbol{f}_0 \cdot \boldsymbol{s} = n + \frac{1}{2}$, the signs alternate, yielding a very small total amplitude. Consequently, the above conclusion remains valid: the image will be modulated by bright fringes obeying the relation $\boldsymbol{f}_0 \cdot \boldsymbol{s} = n$.

The size of the particle displacement is the limiting factor in the above procedure; thus it is necessary to reduce the filter diameter until the bandwidth of the impulse response is greater than the displacement. Increasing the width of the impulse response, however, decreases the resolution and smears the fringes from regions where the velocity is not uniform. This last difficulty, related to the variations of the displacement in the resolution area defined by the impulse response, is the reason why it is difficult to obtain a large number of fringes in regions of high-velocity gradient.

Equation (5.6) shows that the fringes multiply the image of $C(\boldsymbol{r}_0)$. Because the illumination is coherent and $C(\boldsymbol{r}_0)$ consists of a random 'dot' matrix, the corresponding image is modulated by a coherent speckle noise. The noise is caused by interference between the diffracted illumination from the randomly distributed particle images. This phenomenon is the other limitation of the technique and explains the noisy aspect of the fringes. Note that this effect is also the origin of the speckle noise in the Young's fringes obtained by local illumination, but in that case the averaging technique used in processing suppresses the adverse effects.

6. Discussion of the results

6.1. *Measurements of the thermal distribution*

Equilibrium conditions were established in the cavity fluid about two hours after the temperature-control circulators were started. After the start-up transient, the motion in the upper part of the cavity consists of two horizontally elongated cells. These recirculation regions extend across the length of the cavity and are separated by a narrow, unsteady descending plume. Local temperature measurements taken with a 0.13 mm diameter thermocouple at various distances from the endwalls, and throughout the cavity depth, reveal that the bulk of the fluid is isothermal and well mixed; see figure 4. Large temperature gradients exist close to the cavity walls and in the immediate vicinity of the surface. An intermittency which decays with distance from the surface has been noted in the latter measurements; similar observations have been reported by Katsaros *et al.* (1977).

Figure 5 shows the temperature distributions recorded near the surface at two different locations together with the analytical results from (2.2) and (2.5). The scaling between the observed values of z and the ordinate ξ is based on a critical Rayleigh number $R_{\text{crit}} = 10^3$, i.e. $t^* = 31.7$ s. Close to the plume the observations, illustrated with open symbols, are consistently less than those recorded nearer the vertical endwall (closed symbols). In the worst case this difference is as large as 50% but decays with distance from the surface. These data were taken with an electromechanical traverse mechanism and a miniature chromel–alumel thermocouple probe. Local measurements from stationary probes at the corresponding spanwise locations, denoted with crosses, are in reasonable agreement with the dynamic observations. It is therefore concluded that the effect of the recirculation zones is to cause a continuous depletion of some of the relatively cool fluid in the surface thermal layer which is fed into the plume. This process, however, does not prevent the instability from occurring on a timescale that is in fair agreement with the conductive-sublayer model proposed by Howard (1964).

An interferogram which illustrates the horizontal temperature gradients near the plume is shown in figure 6. Continuous observation of the shearing interferometer display for periods up to thirty minutes demonstrated that the plume was always unsteady. The unsteadiness was seen to be a lateral weaving motion intermittently augmented by a vertical plunging of the plume. Measurements of the unsteadiness were obtained from a photo-detector with a pinhole aperture. Regardless of the detector location the mean periodicity was found to be about 30 s, as noted earlier in §2.

6.2. *Velocity data from Young's fringe analysis*

Quasi-steady measurements of the velocity distribution can be made provided the recording time is small compared to the intermittency of the unstable thermal layer. Figure 7 shows a multiple-exposure photograph of the upper region of the test cell.

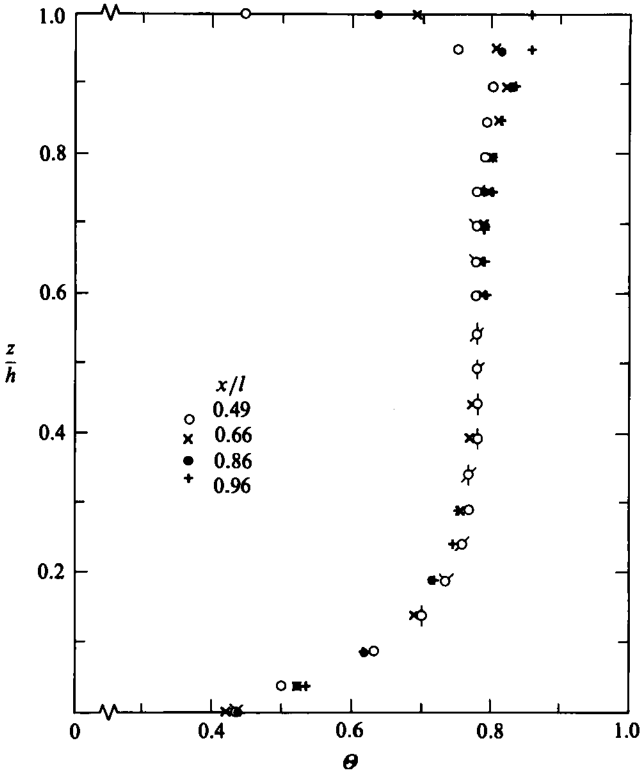

FIGURE 4. Temperature profiles at various locations in the cavity. $R = 1.63 \times 10^7$; $L \approx 1.5$; $\Theta_B \approx 0.42$; $l = 74$ mm; $h = 50$ mm.

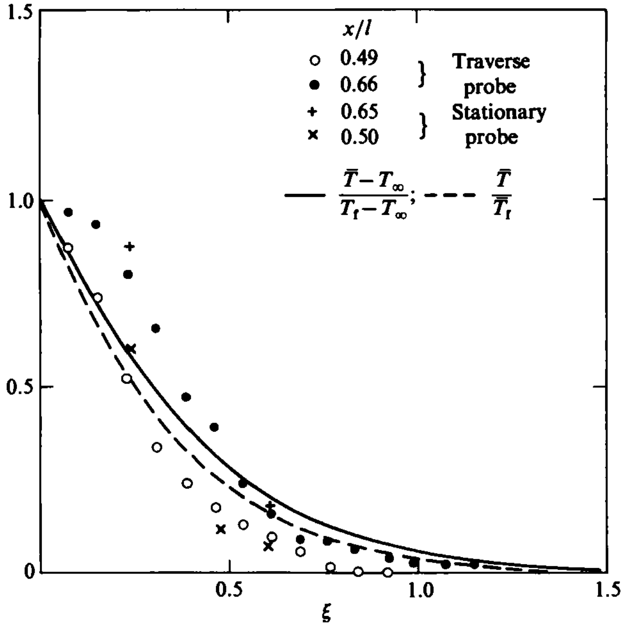

FIGURE 5. Mean temperature profiles near the surface.

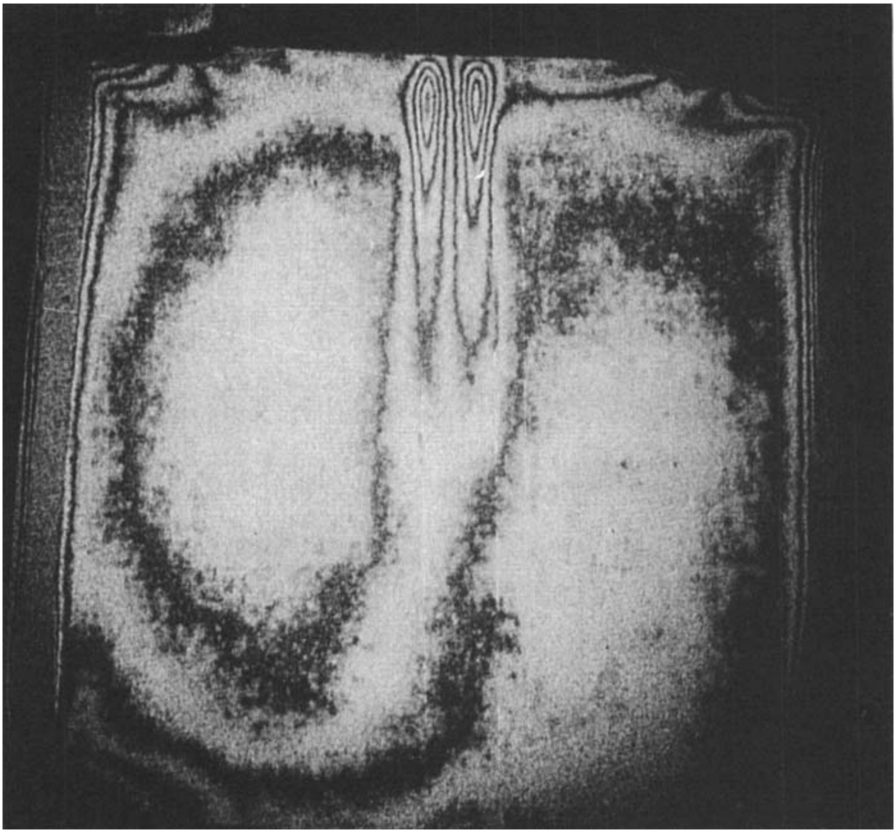

FIGURE 6. Shearing interferogram of the thermal gradients near the plume.

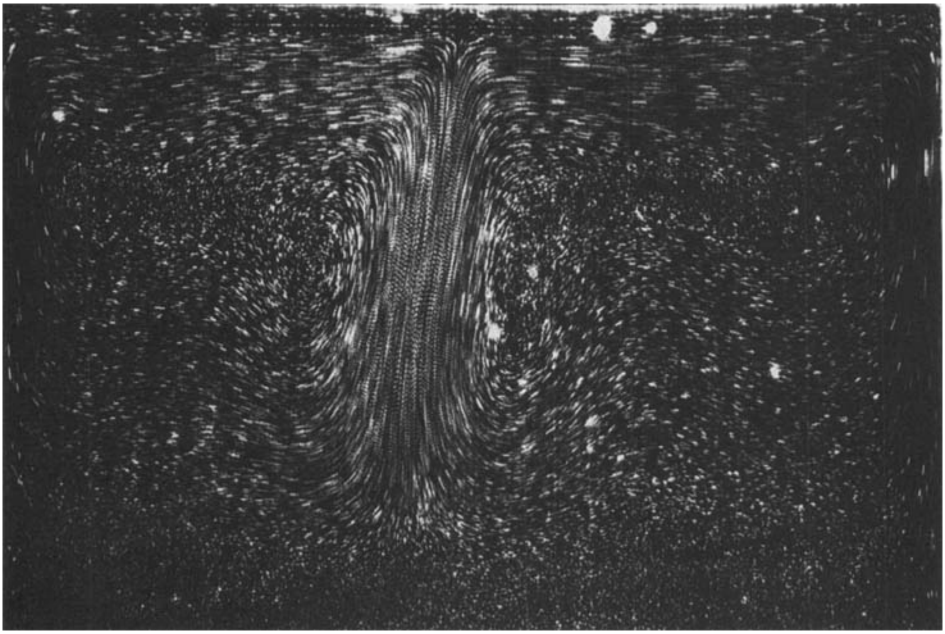

FIGURE 7. Specklegram of the flow field in the upper region. $R = 8.2 \times 10^6$, $L \approx 1$, $\Theta_B = -8.25$.

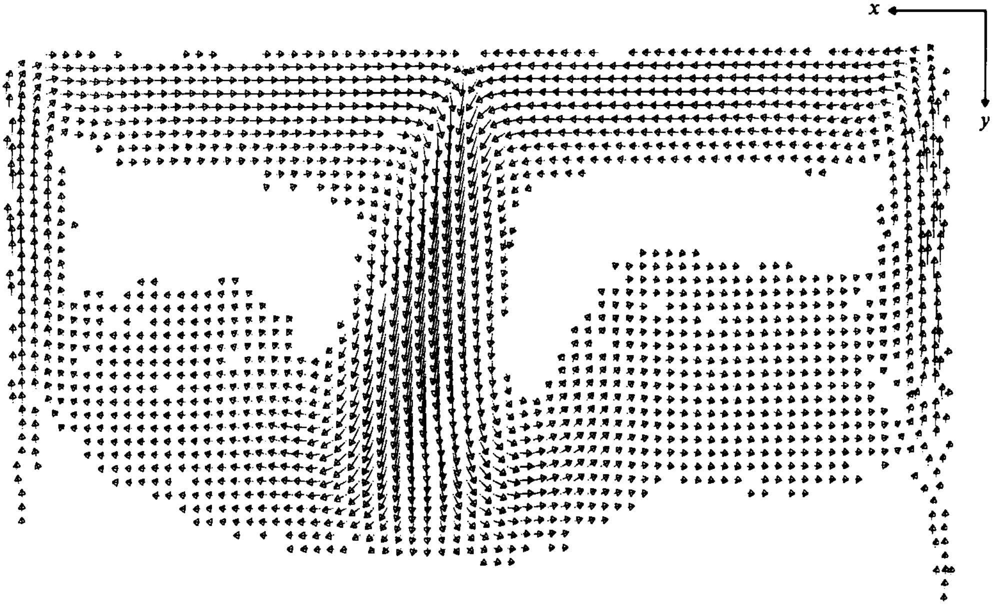

FIGURE 8. The velocity-vector field corresponding to figure 7.

Ten superimposed images, each of 10 ms duration, are recorded in the photograph; the separation time between exposures is 190 ms. Consequently the total exposure time is about 2 s, or less than 7 % of the mean period of the unsteady flow. Note that there is little aberration of the individual particle images due to lateral motion of the plume, which confirms the above assertion.

Results derived by digital-image processing the fringe fields obtained from the specklegram (figure 7) are shown in figures 8 and 9. Data are given for 1981 locations. In the central region of each recirculation cell the motion is too small to be measured from the current records. Local velocity vectors, whose lengths are proportional to the magnitude, are shown in figure 8; the maximum value is approximately 3 mm s^{-1}. Horizontal and vertical velocity components (u, v) were derived from the information in figure 8 and are presented in figure 9 (*a*, *b*), respectively. The discretized data are located on a regular mesh, which corresponds to a sample spacing of about 1 mm. An arithmetic progression is used to subdivide the absolute values into six equally spaced sets ranging from the maximum value of five to zero, and the boundaries between these discrete values are illustrated in figure 9. Flow-field parameters that cannot be measured by the Fourier-filtering technique can be derived from the Young's fringe data in figure 9 (*a*, *b*). For example, the vorticity ζ can be estimated from a knowledge of the velocity component distribution and the grid size, see figure 9 (*c*). Algorithms for deducing the vorticity distribution and estimates of the uncertainty are described in Appendix B.

The above data analyses reveal interesting features of the plume and the recirculation zones. Figure 9 (*a*) indicates that the largest horizontal velocity components occur near the surface and the flow accelerates away from the sidewalls to feed into the plume. In the lower portion of the region, fluid is ejected from the plume over a much broader area and recirculates at a lower velocity. Examination of figure 9 (*b*) reveals that the vertical velocity component is greatest in the plume and that it is moving more rapidly than the fluid near the vertical walls. This observation is

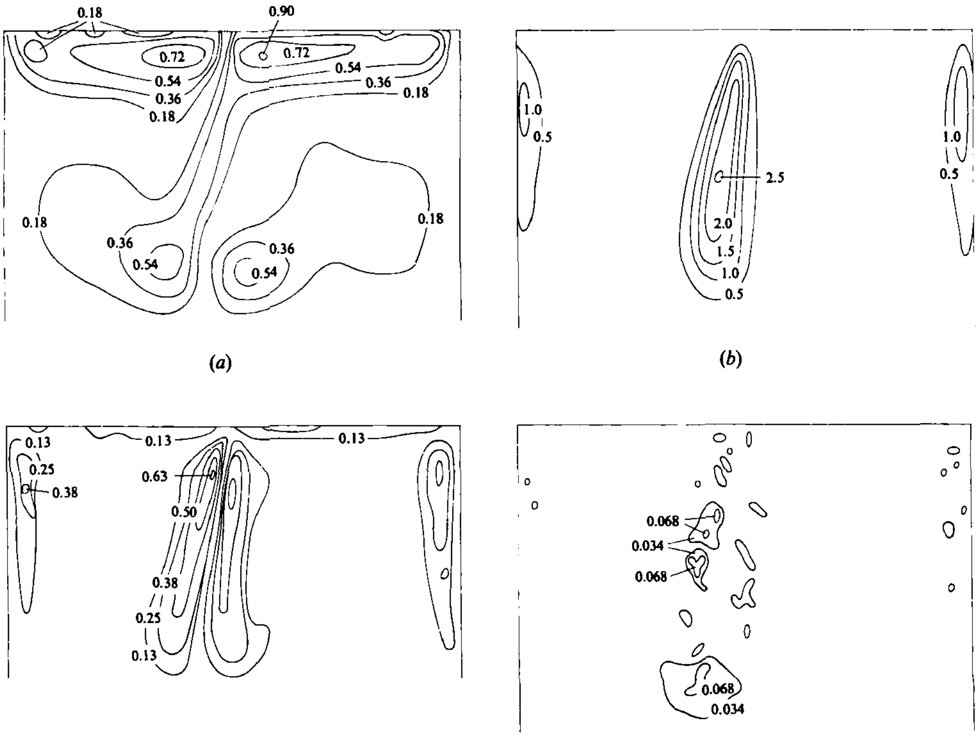

(a) (b)

(c) (d)

FIGURE 9. (a) Horizontal-velocity-component distribution; $u_{\max} \approx 0.9\ \text{mm s}^{-1}$. (b) Vertical-velocity-component distribution; $v_{\max} \approx 2.5\ \text{mm s}^{-1}$. (c) Vorticity distribution; $\zeta_{\max} \approx 0.63\ \text{s}^{-1}$. (d) Estimates for the gradient of the out-of-plane component.

consistent with the measurements in figures 8 and 9(c). One other interesting observation emerges from these data. Incremental differences of the in-plane velocity components can be used to estimate the out-of-plane velocity gradient $(-(\partial w/\partial z) = (\partial u/\partial x) + (\partial v/\partial y))$. For these experiments the estimates show $(\partial w/\partial z) \approx 0$ everywhere except near the bottom of the plume. In this region $(\partial w/\partial z)$ is systematically non-zero, denoting that some three-dimensional motion occurs, see figure 9(d). This deduction is in accord with visual observations, made during the experiments, of a scintillation effect in the same region. An optical effect of this type suggests that particles are passing through the light sheet.

6.3. *Velocity distributions from Fourier filtering*

A series of fourteen speckle photographs together with the corresponding fringe distributions of the horizontal and vertical velocity component is given in figure 10. These pictures were taken at 10 s intervals, and individual frames comprise ten images each of 10 ms duration as described in §4. Each fringe field is the result of Fourier filtering the individual photographs in the manner described in §5.2. Fringes of equal velocity component represent increments of $0.3\ \text{mm s}^{-1}$ in the horizontal direction and $0.81\ \text{mm s}^{-1}$ in the vertical direction. Although considerable lateral movement of the plume can be seen in the sequence, the totality of the frames illustrates that a complete cycle of the motion may occur about a non-vertical plane. The weaving motion of the plume as it descends into the bulk of the fluid is

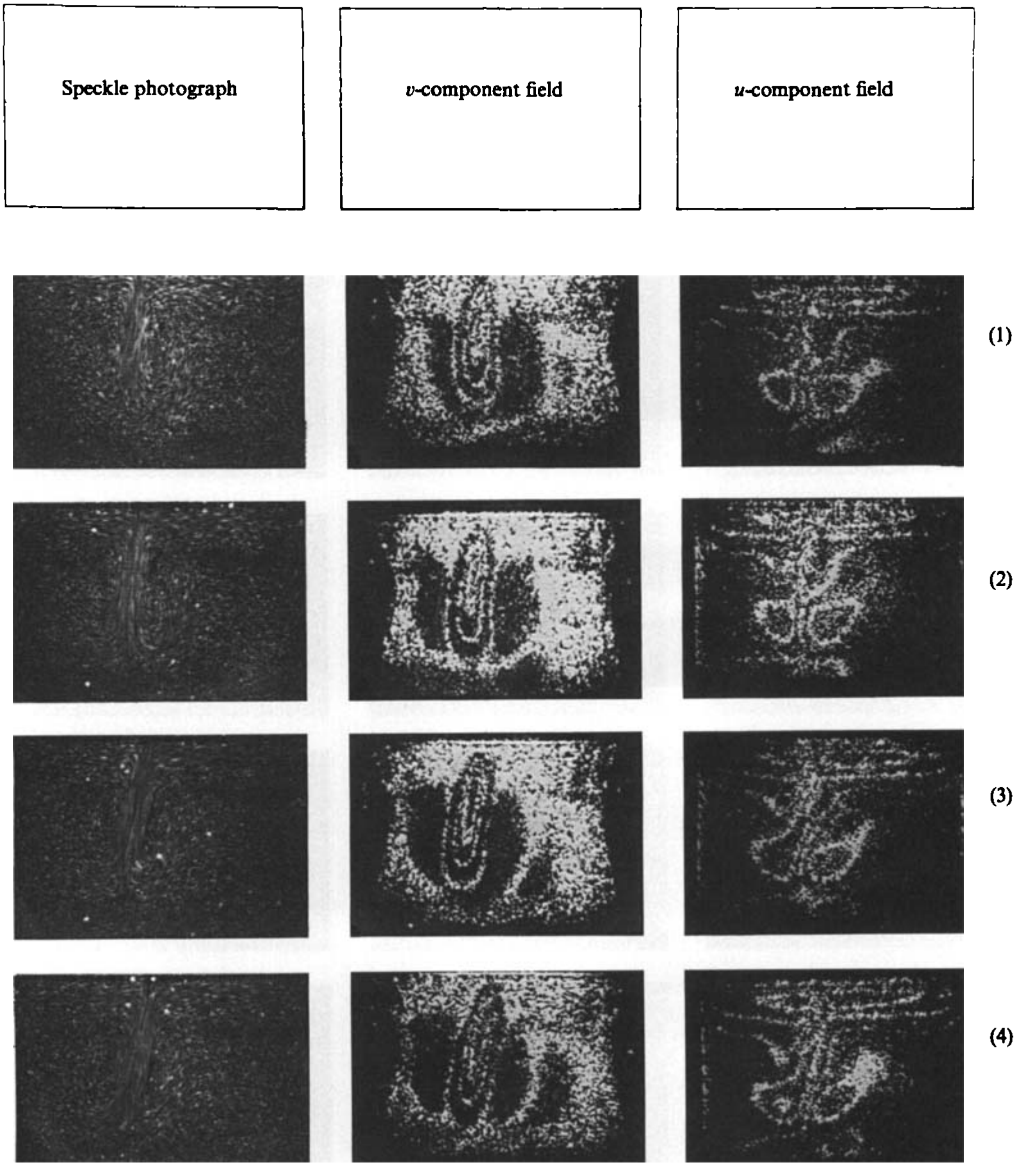

FIGURE 10. For caption see p. 251.

accompanied by a displacement of the surface attachment location, which moves approximately 10% of the cavity length. In general the Fourier-filtered patterns of the velocity components show three or four fringe orders. The horizontal-velocity-component field illustrates the changes that occur in the vicinity of the plume front. Notice that the eye-like regions change position and orientation in a regular and substantial fashion. Complementing this behaviour, the vertical velocity components clearly illustrate the weaving motion of the plume and the growth and contraction of its penetration length.

In §2, it was noted that tilting plumes have been recognized as representing a large-scale motion which develops in shallow cavities beyond a bifurcation at $R^* \approx 2 \times 10^6$. Inspection of numerous photographs taken with exposures between 15

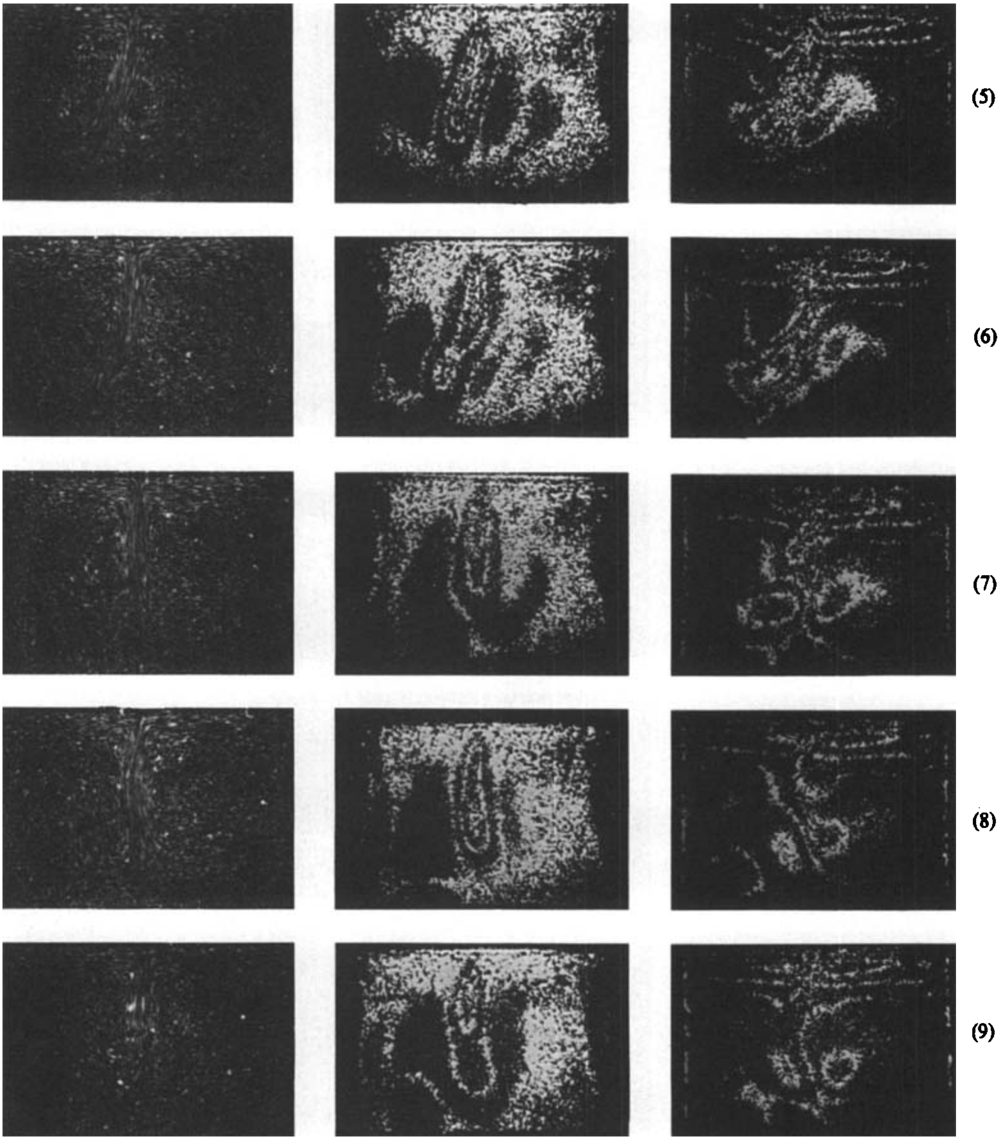

FIGURE 10. (*cont.*) For caption see p. 251.

and 64 s reveals features in the flow similar to those described by Krishnamurti & Howard (1981). For cavities with aspect ratios of $0.7 \leqslant L \leqslant 1.4$, it has been found that one of two states of motion occurs when $R^* \geqslant 10^7$. Either the flow exhibits a vertical plume which is offset from the centreline of the cavity, so that the recirculation cells on each side differ in length; or the non-symmetric cells become progressively distorted with increasing R^* and the plume tilts away from the vertical plane. Since the photographs under discussion are records with relatively long exposure times there is no doubt that the plumes are oscillating about some mean orientation in a manner equivalent to that illustrated in figure 10.

The resemblance between the horizontal-velocity-component contours given in figure 9(*a*) and the corresponding filtered image in figure 10 (frame 13) is not

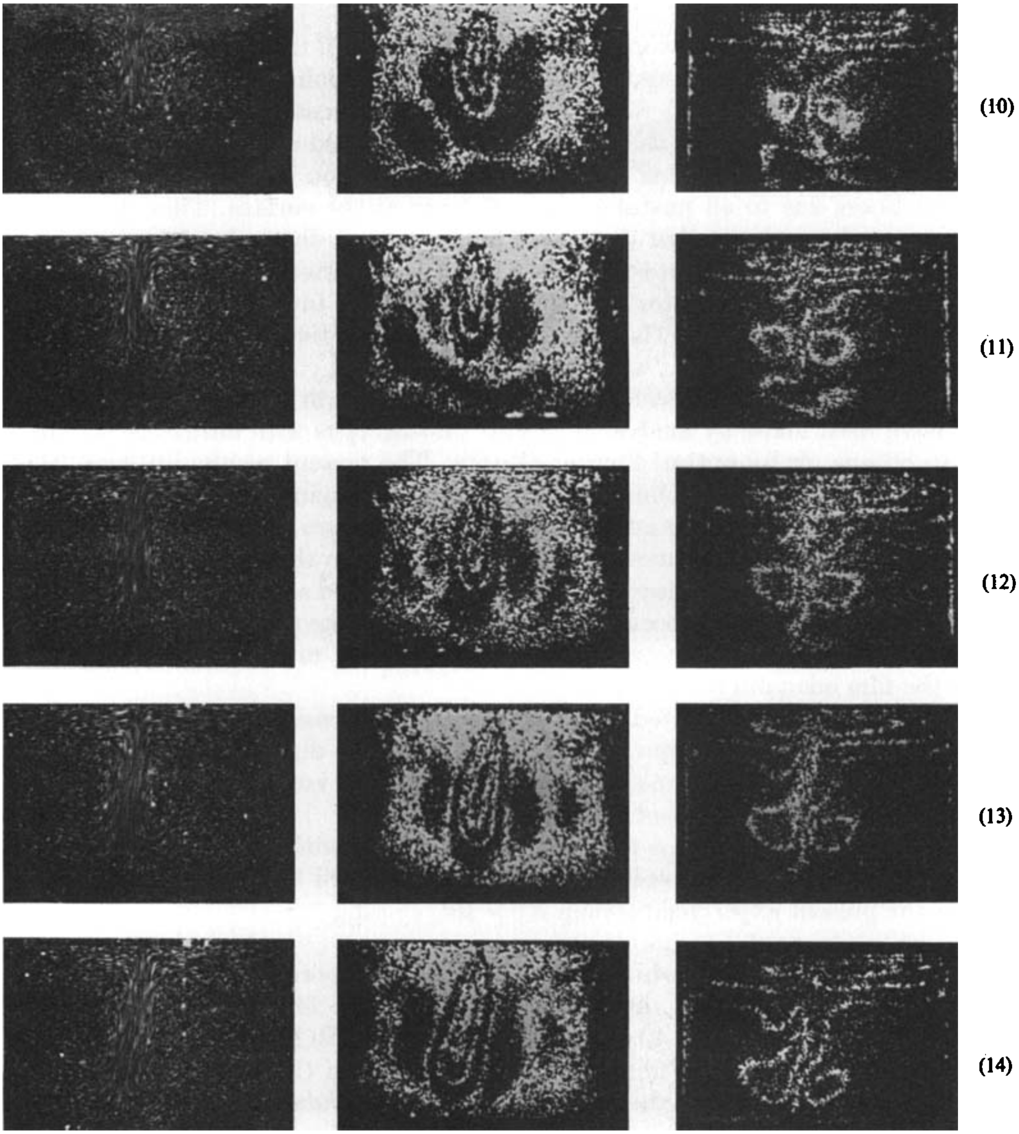

FIGURE 10. Speckle images of the plume, and the corresponding Fourier fields of the horizontal and vertical velocity components. The u-component fringe separation is 0.3 mm s^{-1} and the v-component fringe separation is 0.8 mm s^{-1}.

coincidental. Because the sensitivities used in the two methods of analysis were different, the fringe orders are not identical, but a visual comparison demonstrates that the results exhibit similar characteristics. Synthesized Fourier contour maps can be obtained from the Young's fringe data by highlighting alternate regions in the digitized isovelocity field. This has been done in one particular case for identical sensitivities and the results are convincingly similar.

7. Conclusions

This study has concentrated on a detailed examination of the flow field in the upper portions of a liquid-filled rectangular cavity with surface cooling. Local measurements close to the surface show that the mean temperature across the thermal layer near the plume is consistently less than in similar data recorded elsewhere. Other results have demonstrated that the buoyancy-driven recirculation is locally modulated by an unsteadiness due to an unstable thermal layer at the surface. Time-dependent measurements have shown that the unsteadiness causes a descending plume to have characteristics similar to those associated with turbulent thermals. In particular, the intermittent eruption of the unstable thermal layer feeds into the plume, causing it to penetrate into the cavity. The duration of the conductive phase in the sublayer instability is in fair agreement with the model proposed by Howard (1964).

Quasi-steady measurements of the velocity distribution in the upper regions of the cavity have been made by analysing speckle photographs with either the Young's fringe technique, or by optical Fourier filtering. The present results illustrate that although double-exposure techniques are useful for studying high-speed flows, the multiple-exposure method has advantages for flows that are sufficiently steady. One particular advantage is the increased signal-to-noise ratio that is achieved. Also, as noted in §5.1, very low velocities can be measured with good accuracy by this method. These advantages would also occur with high-repetition-rate pulsed systems provided that the individual pulse-intensity levels are reasonably uniform and sufficient to expose the film adequately.

It has also been demonstrated that digital image processing of the data acquired by the Young's fringe technique yields not only the two-dimensional velocity field and its components, but also meaningful estimates of the vorticity and any velocity gradients in the third dimension.

Lastly, a quasi-steady motion similar to that identified with a bifurcation to a state involving transient tilted plumes (Krishnamurti & Howard 1981), has been found to occur in the present experiments when $R^* > 10^7$.

The experiments were conducted at AT&T Bell Laboratories and the digital analyses were undertaken at the von Kármán Institute for Fluid Dynamics; the support from both of these institutions is acknowledged. R.M. was aided by a grant from the Belgian National Fund for Scientific Research (FNRS). This work was also partially sponsored by the National Science Foundation under Grant No. CBT-8418229.

Appendix A

Multiple-exposure recording reduces the offset Δ caused by the presence of a diffraction halo whose precise intensity distribution is not known. If the signal $f(m)$ is described as the product of a constant-amplitude co-sinusoidal signal $s(m)$ and an unknown envelope $e(m)$, i.e.

$$f(m) = s(m)\,e(m), \tag{A 1}$$

then the extrema m_e of this waveform are the solutions of

$$s(m)\frac{\mathrm{d}e}{\mathrm{d}m} + e(m)\frac{\mathrm{d}s}{\mathrm{d}m} = 0, \tag{A 2}$$

which are different from the solutions m_0 of $\mathrm{d}s/\mathrm{d}m = 0$. Because the offset due to $e(m)$ is small compared to the period of $s(m)$, both $s(m_\mathrm{e})$ and $\mathrm{d}s/\mathrm{d}m|_{m=m_\mathrm{e}}$ may be approximated by first-order expansions in the vicinity of m_0 to give

$$\varDelta = -\left(\frac{\mathrm{d}e}{\mathrm{d}m}\right)_{m=m_0}\left\{e(m_0)\left(\frac{\mathrm{d}^2s}{\mathrm{d}m^2}\right)_{m=m_0}\right\}^{-1}. \tag{A 3}$$

For a doubly exposed photograph, $s(m) = \tfrac{1}{2}(1+\cos mKx)$, where K is a constant of proportionality dependent on the geometry of the system and x is the displacement. In this case, the first maximum $m_0 = 2\pi/Kx$, and the offset

$$\varDelta = \frac{2\left(\dfrac{\mathrm{d}e}{\mathrm{d}m}\right)_{m_0}}{K^2x^2e(m_\mathrm{e})}. \tag{A 4}$$

Equations (A 3) and (A 4) show that the offset $\varDelta$ is inversely proportional to x and can become large when the displacement is small. Note that the relative offset $(\varDelta/m_0) \propto \varDelta x)$ grows as x^{-1}. However, when the number of exposures increases, $\mathrm{d}^2s/\mathrm{d}m^2$ also increases and the effect is reduced. Consequently, the maxima of $f(m)$ are located much more accurately.

Appendix B

Suppose the components (h_x, h_y) of individual particle displacements are stored in matrices $h_x(i,j)$ and $h_y(i,j)$. The vorticity ζ is obtained from the definition

$$\begin{aligned}\zeta(i,j) &= \frac{\partial v}{\partial x}-\frac{\partial u}{\partial y}\\ &\approx (s\Delta t)^{-1}[\tfrac{1}{2}\{h_y(i+1,j)-h_y(i-1),j))\}-\tfrac{1}{2}\{h_x(i,j+1)-h_x(i,j-1)\}],\end{aligned} \tag{B 1}$$

where s is the sampling distance and Δt is the interval between exposures. Occasionally this algorithm cannot be used because data in one or more of the elements are missing. Typically this happens near rigid boundaries. If, for example, the displacement at $(i+1,j)$ is missing, the approximation

$$\frac{\partial v}{\partial x} \approx (s\Delta t)^{-1}[h_y(i,j)-h_y(i-1,j)] \tag{B 2}$$

is used.

The uncertainty in these calculations can be estimated as follows. Since the orientation of α of the fringes is known, if $u > v$ the periodicity along y is measured, yielding h_x: h_y is then found from $h_y = h_x \tan\alpha$. Using (B 1), the uncertainty is given by

$$\Delta\zeta = (s\Delta t)^{-1}[\Delta h_x+\Delta h_x \tan\alpha+\Delta\alpha h_x \sec^2\alpha], \tag{B 3}$$

where $\Delta\alpha$ and Δh_x, are the uncertainties in α and h_x. In a representative situation, $h_x = 100$ μm, $\alpha = 30°$, $s = 0.5$ mm, $\Delta t = 200$ ms, $\Delta\alpha = 1°$ and $\Delta h_x = 5$ μm, yielding an uncertainty of $\Delta\zeta = 0.1\ \mathrm{s}^{-1}$.

In regions where the derivatives are estimated according to (B 2) the error will be twice as large.

REFERENCES

ASUNDI, A. & CHIANG, F. P. 1982 Theory and applications of the white-light speckle technique. *Opt. Engng* **21**, 570.

BURCH, J. M. & TOKARSKI, J. M. J. 1968 Production of multiple beam fringes from photographic scatterers. *Optica Acta* **15**, 101.

BRYNGDAHL, O. 1965 Applications of shearing interferometry. *Progress in Optics IV*, p. 37. North-Holland.

CARSLAW, H. S. & JAEGER, J. C. 1959 *Conduction of Heat in Solids*, chap. 2. Clarendon.

ELDER, J. W. 1968 The unstable thermal interface. *J. Fluid Mech.* **32**, 69.

FOSTER, T. D. 1965 Onset of convection in a layer of fluid cooled from above. *Phys. Fluids* **8**, 1770.

FOSTER, T. D. & WALLER, S. 1985 Experiments on convection of very high Rayleigh numbers. *Phys. Fluids* **28**, 455.

GOODMAN, J. W. 1968 *Introduction to Fourier Optics*, chap. 7, p. 141. McGraw-Hill.

HOWARD, L. N. 1964 Convection at high Rayleigh number. In *Proc. 11th Intl Cong. Appl. Mech., Munich* (ed. H. Görtler), p. 1109. Springer.

HOWARD, L. N. & KRISHNAMURTI, R. 1986 Large-scale flow in turbulent convection: a mathematical model. *J. Fluid Mech.* **170**, 385.

JAUPART, C., BRANDEIS, G. & ALLÈGRE, C. J. 1984 Stagnant layers at the bottom of convecting magma chambers. *Nature* **308**, 535.

KATSAROS, K. B., LUI, W. T., BUSINGER, J. A. & TILLMAN, J. E. 1977 Heat transport and thermal structure on the interfacial boundary layer measured in an open tank of water in turbulent free convection. *J. Fluid Mech.* **83**, 311.

KRISHNAMURTI, R. & HOWARD, L. N. 1981 Large-scale flow generation in turbulent convection. *Proc. Natn. Acad. Sci. USA* **78**, 1981.

LIGHTHILL, M. J. 1953 Theoretical considerations on free convection in tubes. *Q. J. Mech. Appl. Maths* **6**, 398.

LIPSON, S. G. & LIPSON, H. 1969 *Optical Physics*, chap. 7. Cambridge Univesity Press.

LOURENCO, L. M. & WHIFFEN, M. C. 1984 Laser speckle methods in fluid dynamics applications. In *Proc. 2nd Intl Symp. on Applications of Laser Anemometry to Fluid Mech., Lisbon*. Ladoan.

MEYNART, R. 1980 Equal velocity fringes in a Rayleigh–Bénard flow by the speckle method. *Appl. Optics* **19**, 1385.

MEYNART, R. 1982 Convection flow field measurement by speckle velocimetry. *Revue Phys. Appl.* **17**, 301.

MEYNART, R. 1983*a* Mesure de champs de vitesse d'écoulements fluides par analyse de suites d'images obtenus par diffusion d'un feuillet lumineaux. Ph.D. thesis, Université Libre de Bruxelles.

MEYNART, R. 1983*b* Instantaneous velocity field measurements in unsteady gas flow by speckle velocimetry. *Appl. Optics* **22**, 535.

MILLER, D. C. & PERNELL, T. L. 1981 The temperature distribution in a simulated garnet Czochralski melt. *J. Cryst. Growth* **53**, 523.

OERTEL, H. & BÜHLER, K. 1978 A special differential interferometer used for heat convection investigations. *Intl J. Heat Mass Transfer* **21**, 1111.

PICKERING, C. J. D. & HALLIWELL, N. A. 1984 Speckle photography in fluid flows: signal recovery with two-step processing. *Appl. Optics* **23**, 1128.

SIMPKINS, P. G. 1985 Convection in enclosures at large Rayleigh numbers. In *Symp. on Stability in Convective Flows, 106th WAM, Miami, FL* (ed. W. S. Saric & A. A. Szewczyk), p. 39. ASME.

SIMPKINS, P. G. & DUDDERAR, T. D. 1981 Convection in rectangular cavities with differentially heated end walls. *J. Fluid Mech.* **110**, 433.

SPANGENBERG, W. G. & ROWLAND, W. R. 1961 Convective circulation in water induced by evaporative cooling. *Phys. Fluids* **4**, 743.

TOWNSEND, A. A. 1959 Temperature fluctuations over a heated horizontal surface. *J. Fluid Mech.* **5**, 209.

WILLIS, G. E. & DEARDORFF, J. W. 1979 Laboratory observations of turbulent penetrative convection planforms. *J. Geophys. Res.* **84**, 295.